3D Imaging of Lithium Protrusions in Solid-State Lithium Batteries using X-ray Computed Tomography

*Shuai Hao, Josh J. Bailey, Francesco Iacoviello, Junfu Bu, Patrick S. Grant, Dan J. L. Brett and Paul R. Shearing**

Dr. S. Hao, Dr. J. Bailey, Dr. F. Iacoviello, Prof. D. J. Brett, Prof. P. R. Shearing
Electrochemical Innovation Lab, Department of Chemical Engineering, University College London, London WC1E 7JE, UK.
E-mail: p.shearing@ucl.ac.uk

Dr. S. Hao, Dr. J. Bailey, Dr. J. Bu, Prof. P. S. Grant, Prof. D. J. Brett, Prof. P. R. Shearing
The Faraday Institution, Quad One, Harwell Science and Innovation Campus, Didcot OX11 0RA, UK.

Dr. S. Hao, Dr. J. Bailey
Research Complex at Harwell, RAL, Didcot OX11 0FA, UK.

Dr. J. Bu, Prof. P. S. Grant
Department of Materials, University of Oxford, Parks Road, Oxford OX1 3PH, UK.

Keywords: lithium protrusions, solid-state batteries, morphology, X-ray CT, crack

Abstract: Solid-state lithium batteries will revolutionize the lithium-ion battery and energy storage applications if certain key challenges can be resolved. The formation of lithium-protrusions (dendrites) that can cause catastrophic short-circuiting is one of the main obstacles, and progresses by a mechanism that is not yet fully understood. By utilizing X-ray computed tomography with nanoscale resolution, the 3D morphology of lithium protrusions inside short-circuited solid electrolytes has been obtained for the first time. Distinguishable from adjacent voids, lithium protrusions partially filled cracks that tended to propagate intergranularly through the solid electrolyte, forming a large waved plane in the shape of the grain boundaries. Occasionally, the lithium protrusions bifurcate into flat planes in a transgranular mode. Within the cracks themselves, lithium protrusions preferentially located in regions of relatively low curvature. The crack volume filled with lithium in two samples was 82.0 % and 83.1 %, even though they had distinctly different relative densities. Pre-existing pores in the solid electrolyte, as a consequence of fabrication, could also be part-filled with lithium, but did not have a

significant influence on the crack path. The crack/lithium-protrusion behavior qualitatively supports a model of propagation combining electrochemical and mechanical effects.

1. Introduction

The solid-state lithium battery is considered one of the most promising candidates for future batteries because a lithium anode will maximize specific energy density and the non-flammable solid electrolyte will dramatically improve safety. The solid electrolyte can also be expected to mechanically block lithium propagation, especially for inorganic solid electrolytes that have relatively high shear modulus,[1] thereby removing a serious challenge impeding the implementation of metallic electrodes. However, it has also been widely reported that lithium can nonetheless nucleate and propagate through dense solid electrolytes and lead to a short circuit when the current density is higher than a critical value, in almost all kinds of solid electrolyte, including organic polymer electrolytes[2, 3] and inorganic electrolytes (oxide[4-6] and sulphide[7, 8]).

Therefore, a great deal of work has focused on understanding lithium protrusions (elsewhere referred to as dendrites, following the convention from liquid electrolytes; here, we use "lithium protrusions" instead, as the lithium distribution in solid electrolyte are not classically "dendritic" from a geometrical definition), including modelling nucleation[9-12] and experimental strategies for their suppression[13-15] and so on. To fully understand the formation and growth mechanism, it would be enormously helpful to evaluate the morphology of lithium protrusions inside the solid electrolyte. However, it is challenging to detect lithium features that are "buried" inside the solid electrolyte. Whilst many techniques have been utilized, including optical microscopy,[16-18] scanning electron microscope (SEM),[6, 19-22] nuclear magnetic resonance (NMR),[23] neutron depth profiling,[24, 25] most of them provide only 1D or 2D information of the lithium protrusion, and the apparently complex three-dimension morphology cannot be resolved. For example, in most SEM images, 2D cross-sectional images of the solid electrolyte are obtained, showing lithium protrusions located in narrow cracks.[5, 6, 20-22] However, with the

limitation of the depth of field, only the surface of the sample can be observed, and consequently understanding of how the lithium protrusions and cracks extend and propagate inside the solid electrolyte is limited. Moreover, the solid electrolytes typically have to be broken in order to expose internal cross-sections,[20-22] during which the lithium distribution at the testing surfaces may be disturbed. Without clear experimental image and data of the lithium protrusions and how they propagate in practice, the value of simulation and theoretical studies is limited.

X-ray computed tomography (CT) provides a technique by which the 3D morphology of the internal structure can be non-destructively investigated and quantitatively analyzed. However, in solid electrolytes, traditionally only the cracks and pores, but not the lithium protrusions, can be imaged,[3, 26, 27] as a number of challenges persist for distinguishing the lithium protrusions from their adjacent voids in cracks and pores. Firstly, the image contrasts of lithium and voids are similar, especially when they locate inside dense solid electrolyte; this is caused by the low X-ray absorption coefficient of lithium, which is close to that of air. Secondly, the X-ray energy needs to be significantly increased in order to penetrate the dense solid electrolyte, especially for high-density garnet electrolytes composed of several heavy elements (La, Zr and doped elements, such as Ta, W, Ga and so on). Unfortunately, this is in opposition to the preferred low-energy, phase contrast techniques that have been typically used for lithium imaging.[28, 29] This creates a dilemma that makes it very challenging to distinguish separately the morphology of lithium protrusions, cracks, and intrinsic pores. Finally, there is a trade-off between sample size and resolution, which is challenging for resolving fine-scale microscopic cracks.

In this study, by utilizing high-resolution X-ray nano-CT at comparatively low X-ray energy and decreasing the sample size to the micron-scale, the morphology of lithium protrusions in short-circuited garnet-based solid electrolytes is successfully distinguished and isolated in three dimensions for the first time. We show clear 3D images of how lithium partially fills cracks and prefers to propagate along grain boundaries, forming a large waved plane. Two garnet

electrolytes with different relative densities are studied and the distribution of lithium protrusions in cracks and pores compared.

2. Result and Discussion

2.1. Characterization of the LLZTO pellet

Doped $Li_7La_3Zr_2O_{12}$ was selected as a model solid electrolyte material as it is amongst the most electrochemically stable solid electrolytes vs. lithium metal, with negligible interfacial reactions. The first solid electrolyte sample, sintered by a conventional route, comprised single-phase cubic $Li_{6.6}La_3Zr_{1.6}Ta_{0.4}O_{12}$ (LLZTO) with a grain size of 2-3 μm, confirmed by X-ray diffractometry (XRD) and SEM (shown in Figure S1a-b). After polishing, the surfaces of the pellet were flat and smooth but with small pores located at the juncture of several grains (Figure S1c). The relative density of the pellet was 90.9%. After assembly in a symmetrical cell (Li/LLZTO/Li), the cell was cycled until a short circuit occurred and then disassembled to recover the solid electrolyte pellet. To promote lithium protrusion growth, no Li/LLTZO thin interfacial layer (such as Au, inorganic, polymer, oxide ceramic etc) was applied and no liquid electrolyte was added.

As shown in the optical micrograph in Figure 1a, a long black line growing through the pellet was observed on both sides. Similar features have been widely reported[22, 26, 30-32] and were identified as the trajectory of lithium protrusions. Figure 1b shows the black line viewed from the top surface of the pellet in an SEM operated back-scattered electron (BSE) mode. After cutting the pellet perpendicular to the lithium protrusion, its morphology was also revealed in cross-section under both secondary electron (SE) and BSE modes, as shown in Figure 1c and 1d respectively. Based on different imaging mechanisms, the BSE mode can distinguish different elements in image contrast and has widely been used to view lithium,[18, 20, 22] as a complement to the morphological information from SE mode. Combined these images, it indicates a narrow crack and a small terrace filled with lithium. Among the X-ray energy

dispersive spectroscopy (EDS) maps in Figure 1e-h, as lithium falls outside the detection range, no element is detected in the crack, while other elements disperse in other areas. Similar lithium features have previously been confirmed using Auger electron spectroscopy[31] and NMR.[22]

2.2. 3D images by slice-and-view

A cross-section of the LLZTO pellet beneath the crack (the black line) location was then imaged by a "slice-and-view" procedure in a focused-ion beam scanning electron microscopy (FIB-SEM) system (JIB-4700F) using secondary electrons (SE). Before the investigation, a thin layer of Pt was deposited on the surface of the region of interest; the cross-section was sequentially milled using a Ga^+ ion beam and imaged by SEM, as schematically shown in Figure 2d. The SEM images at different milling depths are shown in Figure 2a-c. There was a thin layer of lithium directly underneath the platinum layer, which was a remnant from the lithium electrode adhered tightly onto the LLZTO pellet. A long crack originated from the surface of the LLZTO pellet and propagated toward the bottom right corner of the pellet, with interconnecting pores in some areas. Near the surface of the pellet, there were many small cracks extending between the long crack and the surface, which have been suggested to be induced by internal stresses due to lithium-protrusion propagation in the brittle LLZTO.[33] The larger pore was partially-filled with solid material, as indicated by the red arrows in Figure 2a-b. According to previous reports[22] and an image contrast that is characteristic of a low-Z material, it can be surmised that lithium partially fills the pore. Although lithium might be expected to fill both cracks and pores, it was however hard to distinguish lithium explicitly inside these narrow cracks. After reconstructing the serial SEM images and segmenting the cracks and pores from the LLZTO bulk on the basis of grey level, the long crack could be resolved as propagating as a wavy plane, as shown in the 3D image reconstruction in Figure 2e and **Video 1**. The width of the long crack was < 1 μm and varied along the crack length. In some areas the crack separated into two branches (as shown in **Video 1**) and passed through a total of three pores.

Overall, the lithium protrusion could not be readily segmented and distinguished from cracks and pores because of the relatively large depth of field in the SEM images. The grey-scale at each pixel included contributions from the sample at different depths, and therefore it was difficult and likely inaccurate to distinguish between different phases based solely on image contrast. Therefore, in the following section, non-destructive X-ray CT based on different imaging principle was used to further investigate and reconstruct the detailed morphology of lithium within cracks and pores.

2.3. 3D images by micro and nano X-ray CT

A small pillar of ca. 270 μm diameter containing the crack was removed from the bulk LLZTO sample by laser micro-machining. When subsequently imaged by X-ray micro-CT, a blurry crack was revealed in the approximate middle of the pillar (Figure S2); however, the resolution and transmission were insufficient to reveal any further detail. Therefore to obtain higher resolution, the size of the pillar was gradually decreased by FIB milling, as shown in Figure S3a, eventually achieving a fine pillar of ca. 10 μm diameter, as shown in Figure S3b. During the cutting process, care was taken to ensure the crack was retained within the fine pillar, as shown in the inset in Figure S3b.

X-ray nano-CT was conducted using a ZEISS Xradia 810 Ultra. The small pillar was rotated through 180° while capturing radiographic projections that were subsequently reconstructed in 3D using a filtered back-projection algorithm (Zeiss XM Reconstructor). A high-resolution imaging mode was utilized to achieve a voxel size of 32 nm. In Figure 3a, a virtual slice extracted from a plane perpendicular to the axis of the pillar shows long cracks growing through the pillar, together with a pore at the juncture of several grain boundaries. It is worth noting that the greyscale along the cracks was different, as clearly illustrated in Figure 3c by a line profile of the greyscale corresponding to a red line marked in Figure 3b. Based on the Beer-Lambert Law, in one virtual slice the grey level is determined by the linear attenuation coefficient of different constituent materials. Inside the cracks, the lighter part corresponded to lithium

protrusions and the darker part corresponded to remaining voids, indicating that the crack was only partially filled with lithium. In this imaging set-up, contrast between lithium and adjacent voids (voids are defined here as unfilled space in cracks and pores, and distinct from the pores themselves) was improved because the X-ray interaction with lithium was increased by using a comparatively low X-ray energy of 5.4 keV. As shown in Figure 3d, based on the difference in greyscale, lithium, voids and LLZTO could be clearly segmented, and are rendered in grey, red and yellow respectively.

Cross-sectional slices after three-phase segmentation extracted from orthogonal directions are shown in Figure 3e and f. Again, they show a long crack with bifurcations in some places; the width of the major crack was ca. 0.47 μm, whilst the narrowest detectable branch was only 0.12 μm thick. Figure 3e shows that cracks propagated in a relatively tortuous path within the solid electrolyte. Considering the grain size of LLZTO was 2-3 μm (Figure S1b-c), Figure 3e suggests that the cracks tended to grow along grain boundaries and propagate along – or were templated to – the different orientations of the grains. Meanwhile, other parts of the cracks had relatively long, straight trajectories in Figure 3f, which are suggested to result from transgranular growth. Three orthogonal slices and the volume rendering of the pillar are shown in Figure 3g and 3h respectively, illustrating the crack morphology in three dimensions, as well as the distribution of lithium protrusions and voids within cracks. This is the first time known to the authors that the distribution of lithium protrusions inside the solid electrolyte has been resolved in such detail.

To visualise the crack and associated lithium distribution further, the LLZTO phase can be shown in transparent light yellow so that lithium protrusions are clearer, as shown in Figure 4a-c. Then, by displaying the lithium protrusion in transparent yellow, voids are also clearly depicted in Figure 4d-f. The 3D structures of different phases are also separately displayed in **Video 2**. By comparing these images, the location and distribution of lithium protrusions and voids within partially filled cracks was revealed. Although the lithium protrusions, together

with cracks, bifurcate in some places, overall they form a thin waved and rippled plane. As grain boundaries are considered as the preferential region for lithium-protrusion growth, reported in both experimental[20, 31] and modelling studies,[10, 34] this rippled plane shape is largely templated from the geometry of LLZTO grain boundaries. Forming a macroscopic feature (Figure 1a), the planar lithium protrusions grow through the solid electrolyte, eventually short-circuiting the battery.

Comparing the images of voids with (Figure 4a-c) and without lithium protrusions (Figure 4d-f), the lithium protrusion(s) are shown to almost completely cover the exposed grain surfaces. This indicates that the lithium protrusions tend to fill the crack from the crack walls (the surfaces of the cleaved grain boundaries), and often leave unfilled voids in the central crack regions. Similar phenomena is also observed in SEM images recently reported.[18] As shown in Figure 4d-f, these unfilled voids preferentially appeared at positions where the crack was templated along a different grain orientation or in regions of relatively large curvature. Therefore, to a significant extent, the grain structure controlled the crack shape, which in turn influenced the distribution of lithium and the residual voids inside cracks.

A large pore with a diameter ca. 3 um at the juncture of several grains was partially filled with lithium, as shown in the lower-right corner of Figure 4a and 4d, in qualitative agreement with the FIB-SEM images (e.g. Figure 2a-b) and a similar phenomenon has been previously reported based on 2D SEM images.[18, 22] **Figure 4** shows that the long crack propagated beside the large pore, rather than through it. There was another pore nearby and a further pore next to the long crack shown in the lower-left and at the top of Figure 4a and 4d, respectively. This propagation path suggests that larger pores in the microstructure, at least in the field of view here, had no significant influence on the growth path of cracks and lithium protrusions. Considering the relatively small size of the sample, this influence needs to be investigated further in a larger region; noting the trade-off between sample size and image resolution. Some small pores were also part-filled with lithium (Figure 4d-f). Although these pores seem to be

isolated in the images, they can actually be connected by grain boundaries (as the pores located at the juncture of different grains) or small cracks. Limited by the capacity and resolution of the X-ray CT in this experiment, those grain boundaries and cracks were not resolved, but could act as the diffusion paths for lithium ions and electrons. Besides, as there were no more resolvable cracks in the vicinity, we suggest that any stress induced around the crack was largely relieved by the main crack propagation rather than formation of new cracks. Additional stresses may be present in the solid electrolyte arising from the high temperature sintering process and subsequent cool down, and these stresses interacted with the stress field ahead of the crack in a complex fashion.

By considering the volume fraction of the different materials (LLZTO, lithium protrusions and voids) calculated from segmentation, 82.0 % of the space occupied by the cracks was filled with lithium, while only 57.3 % of the pre-existing pores were filled. The volume of lithium inside cracks was also larger than that accumulated in pre-existing pores. These data indicated that, at least in the volume studied here, lithium preferentially deposited as lithium protrusions in propagating cracks and a smaller amount deposited inside the pre-existing pores; it is hoped this insight will be of value to guide modelling studies of lithium mobility in solid state batteries. However, the degree to which lithium filled features probably varied along cracks and/or within different regions according to changes in the local microstructure (crack width and shape, the number and size of pores nearby and so on).

The growth direction of lithium-protrusions/cracks with the “waved” plane morphology were not noticeably induced or influenced by the pre-exiting pore distribution, which suggests that lithium propagation cannot be prevented simply by decreasing solid electrolyte porosity. Indeed it is known that short circuits occur in LLZO pellets at higher relative density (although the critical current density may be increased[35]). Furthermore, even when pre-exiting pores and grain boundaries are absent, for example in single-crystal LLZO, cracks and lithium protrusions may still result.[17]

To investigate further the influence of pre-existing pores and the relative density of the solid electrolyte, a second LLZTO pellet of higher relative density (98.3%) was prepared using field assisted sintering. Following the same procedure of cycling to a short circuit, the morphology of the lithium protrusion inside was imaged under the prior protocols and settings. The XRD and SEM characterization and cycling performance are shown in Figure S4 and S5. As shown in **Figure 5** and **Video 3**, the lithium protrusions again had a "waved" plane morphology, qualitatively similar to the previous case, and again with no strong preference for propagation related to the distribution of pre-existing pores. This confirmed that the porosity and relative density of the as-manufactured solid electrolyte was not the principal factor affecting lithium-protrusion/crack growth. Improving the density of the solid electrolyte may delay short circuit but would likely not eliminate it.

Again, crack and lithium propagation predominantly followed grain boundaries (here the grain size was 3-5 μm, Figure S4b). It is worth noting that **Figure 5** shows an intergranular lithium-protrusion/crack with a branch indicated by yellow arrows (Figure 5a-c) that was straight and flat, indicating transgranular growth. Therefore, while lithium protrusions generally preferred to propagate along grain boundaries, transgranular crack branches were also occasionally observed.

The width of the major crack was ca. 0.84 μm and the branch width was 0.31 μm, which is approximately twice that of the previous sample. Lithium occupied 83.1 % of the space inside the cracks, similar to the lower density sample. Within the sample, the crack width and extent of lithium filling may change along the crack in different regions. The lithium protrusions, again, preferentially deposited over the exposed crack walls leaving voids in the middle, which is also shown in the SEM image of the pillar (Figure S5). Voids unfilled by lithium within the cracks were in regions of larger curvature or crack deviation, as shown in Figure 5d-f.

The possible process of lithium-protrusion formation and crack growth until short circuit can be schematically shown in **Figure 6** and summarized as follows: at the beginning of the

electrochemical process, a proportion of the lithium deposits at surface flaws or defects, protruding into grain boundaries (Figure 6b). Cracks propagate preferentially along grain boundaries[10, 34] driven by combined electrochemical-mechanical stresses.[12, 17] In some instances, cracks can propagate quickly, presumably due to the low fracture toughness of LLZTO[36] and/or a local superimposed pre-existing or residual stress state. In this case, the crack tip has yet to fill with lithium (Figure 6c). Then, lithium fills the empty crack tip preferentially covering the exposed crack walls as favourable nucleation points.[37] Or, lithium may be molten under high local Joule heating[16] which is then able to flow into the crack, leaving voids behind (Figure 6d). Meanwhile, further behind the crack tip and as the crack continues to open, the pre-deposited lithium are pulled apart, leaving voids in central crack regions. Because of the preference for crack propagation along grain boundaries most of the time, the lithium protrusions are templated by the shape of grain boundaries, although in certain positions, they form branches in a transgranular mode. This process continues until the cell is short-circuited, as shown in Figure 6e.

In general, lithium-protrusion growth and crack propagation are complex phenomena, coupling electrochemical and mechanical processes, and their integrated effect needs to be investigated and rationalized further. The mechanical properties of the solid electrolyte will play an important role. Additionally, it is possible that the mechanism of lithium-protrusion propagation may be different in the early stages than in later stages where a small number of well-developed relatively large cracks are established.

3. Conclusion

Here, for the first time, the 3D morphology of lithium protrusions inside solid electrolyte LLZTO has been revealed by X-ray CT. A combination of FIB-SEM and low-energy nano-CT confirmed the presence of partially filled cracks; in the latter, the enhanced image contrast facilitated three-phase segmentation of the lithium, cracks and the LLZTO. The detailed 3D

morphology of lithium protrusions has been reconstructed, as well as resolution of voids within the lithium that filled the cracks, for two different LLZO relative densities. The lithium protrusions primarily propagated intergranularly through the solid electrolyte, forming a waved plane in a geometry largely templated to the grain boundaries. Lithium protrusions also occasionally formed flat branches in a transgranular mode, typically at complex geometrical features such as grain triple points. Lithium, which partially filled the cracks, tended to locate in regions of relatively low curvature. Unfilled voids preferentially appeared in regions of larger curvature or crack deviation. Some pre-existing pores (as a consequence of fabrication) were also partially-filled with lithium; however, they did not have a significant influence on the growth path of cracks. Given the propensity for grain boundary propagation (but not always), slowing grain boundary diffusion and/or strengthening or toughening grain boundaries may delay lithium protrusion propagation; the work here does not suggest increasing relative density alone would significantly influence propagation behaviour. A possible mechanism of lithium-protrusion/crack growth has been proposed with coupling of electrochemical and mechanical processes. It indicates that both the electrochemical driving force and mechanical properties of the solid electrolyte have a combined effect on the lithium-protrusion/crack propagation and their morphology. These findings enrich the understanding of lithium propagation in solid electrolytes and it is hoped they will be of use in theoretical and modelling research on lithium-protrusion propagation. The methodologies proposed motivate more research on the mechanism of lithium protrusion growth. The same approach can also be used to explore the effectiveness of various strategies for lithium protrusion suppression.

4. Experimental Section

Materials, Battery Assembly and Electrochemical Cycling: Conventionally sintering of LLZTO: Ta-doped LLZO ($Li_{6.6}La_3Zr_{1.6}Ta_{0.4}O_{12}$, LLZTO) powder (Toshima Mfg Co., Ltd.) was ball-milled at 450 rpm for 2 h in isopropanol with ZrO_2 beads as the milling media. After drying

at 60 °C overnight, the powder was uniaxially pressed into pellets with a diameter of 13 mm by a stainless-steel die (Specac Ltd.). The pellets were then calcined at 1250 °C for 10 min in argon, fully covered by the LLZTO mother powder. After cooling, the pellets were polished with 400, 800 and 1200 grit SiC paper in sequence and then transferred into a glovebox.

Field assisted sintering technique (FAST) of LLZTO: $Li_{6.4}La_3Zr_{1.4}Ta_{0.6}O_{12}$ powder (MTI Corp., USA) was loaded into a graphite die set with diameter of 16 mm. The die was transferred into the FAST chamber (DSP 507, Dr Fritsch GmbH & Co. KG, GER), sealed and evacuated immediately. Under a uniaxial pressure of 50 MPa, the die temperature increased rapidly to 1100 °C at 100 °C min^{-1}, and then at 50 °C min^{-1} to the sintering temperature of 1150 °C for 15 min. The pressure was then removed and die cooled naturally to room temperature. The sintered LLZTO pellet was polished using 400-2500 grit SiC paper with isopropanol, cleaned by ultrasonication for 2 min and then transferred into a glovebox.

Symmetric Li/LLZTO/Li electrochemical Swagelok cells were assembled in an Ar-filled glovebox. No liquid electrolyte was added to the cell in order to isolate the reaction between solid electrolyte and lithium. The cells were cycled with a potentiostat (Interface 1000E, Gamry Instruments) at a current density of 0.05 mA cm^{-2} at room temperature. After the cell short-circuited, it was disassembled in a glovebox, and the residual lithium electrode peeled off. The galvanostatic cycling data is shown in the Supplemental Information (Figure S1d and Figure S4d).

SEM and EDS: The microstructure and elemental analysis of the samples were examined in a scanning electron microscope (Zeiss EVO 10, Carl Zeiss Inc., Cambridge, UK) coupled to an energy-dispersive X-ray spectrometer (Oxford x-act, Oxford Instruments, Oxfordshire, UK). SEM images were obtained at an acceleration voltage of 15 kV and a 7.5 mm working distance. Different magnifications were used under SE and BSE modes. The EDS spectra were acquired and treated using the INCA suite software (Version 5.05) (Oxford Instruments, Oxfordshire, United Kingdom).

FIB-SEM: Consecutive cross-sectional images of lithium protrusions in the solid electrolyte were obtained by a dual beam FIB-SEM (JIB-4700F, JEOL Ltd., Tokyo, Japan). A platinum layer was deposited on the top of the sample by in-situ ion-beam-induced deposition to minimize curtaining artefacts. Before the serial sectioning, trenches were milled with a coarse Ga+ ion beam current (Beam 03, 30 nA). Then, consecutive sectioning was performed with a low current (Beam 07, 500 pA) at 30 kV and an incremental step of approximately 0.06 μm. 3D reconstruction of the sample was performed with stacks of 154 images. The image processing was carried out in ImageJ software for alignment and segmentation.

Laser micro-machining: Using laser micro-machining (A Series/Compact Laser Micromachining System, Oxford Lasers), a small cylinder was cut out from the LLZTO pellet.[38] The cylinder was glued onto a 1 mm dowel pin using an epoxy adhesive. The top of the cylinder was milled down to a diameter of ca. 270 μm. After micro-CT test, the sample was milled to a diameter of ca. 100 μm.

After this laser micro-machining step, the sample was gold-coated and then further milled using the Ga+ ion beam described previously. A fine pillar with a diameter about 10 μm was obtained on top of the small cylinder with different ion beam currents from 90 nA (Beam 01) to 10 nA (Beam 04).

X-ray computed tomography and Reconstruction: A lab-based X-ray nano-CT instrument (Zeiss Xradia 810 Ultra, Carl Zeiss Inc., CA, USA) was utilized to characterize the 3D structure of lithium protrusions at the nanoscale. The X-ray beam was generated from a rotating Cr anode with an accelerating voltage of 35 kV and a current of 25 mA. Using a reflective capillary condenser, a quasi-monochromatic X-ray was obtained at the Cr-Kα emission peak of 5.4 keV and projected onto a 1024 × 1024 pixel CCD detector through a Fresnel zone plate. The X-ray absorption-contrast imaging was performed in “High Resolution” mode with 2-voxel binning, resulting in a pixel size of 32 nm and a field-of-view of 16 μm × 16 μm. The fine pillar of LLZTO was rotated through 180° and 1001 radiographs were collected at angular intervals at

an exposure time of 56 s. The projection dataset was reconstructed into a 3D volume in the Zeiss XMReconstructor software (Carl Zeiss Inc.) implemented with a filtered back-projection algorithm for a parallel beam. The 3D volume analysis was carried out in Avizo software (Thermo Fisher Scientific, Waltham, Massachusetts, U.S.) for filtering and segmentation. Based on the different ranges in grayscale, as shown in Fig 3c, the LLZTO, lithium and voids were segmented by the threshold tool in the software.

Supporting Information
Supporting Information is available from the Wiley Online Library or from the author.

Acknowledgements
The authors acknowledge the financial support from the Faraday Institution All-Solid-State Batteries with Li Anode (EP/S003053/1, FIRG007) and the EPSRC (EP/P009050/1), P.R.S. acknowledges the support of The Royal Academy of Engineering (CIET178/59). FIB-SEM experiments were carried out at the Research Complex at Harwell, UK.

Conflict of Interest
The authors declare no conflict of interest.

Received: ((will be filled in by the editorial staff))
Revised: ((will be filled in by the editorial staff))
Published online: ((will be filled in by the editorial staff))

References

[1] C. Monroe, J. Newman, *J. Electrochem. Soc.* **2005**, *152*, A396.

[2] M. Dolle, L. Sannier, B. Beaudoin, M. Trentin, J. M. Tarascon, *Electrochem. Solid-State Lett.* **2002**, *5*, A286.

[3] K. J. Harry, X. Liao, D. Y. Parkinson, A. M. Minor, N. P. Balsara, *J. Electrochem. Soc.* **2015**, *162*, A2699.

[4] K. Ishiguro, H. Nemori, S. Sunahiro, Y. Nakata, R. Sudo, M. Matsui, Y. Takeda, O. Yamamoto, N. Imanishi, *J. Electrochem. Soc.* **2014**, *161*, A668.

[5] Y. Ren, Y. Shen, Y. Lin, C. W. Nan, *ACS Appl. Mater. Interfaces* **2019**, *11*, 5928.

[6] B. Wu, S. Wang, J. Lochala, D. Desrochers, B. Liu, W. Zhang, J. Yang, J. Xiao, *Energy Environ. Sci.* **2018**, *11*, 1803.

[7] M. Nagao, A. Hayashi, M. Tatsumisago, T. Kanetsuku, T. Tsuda, S. Kuwabata, *Phys. Chem. Chem. Phys.* **2013**, *15*, 18600.

[8] S. H. Kim, K. Kim, H. Choi, D. Im, S. Heo, H. S. Choi, *J. Mater. Chem. A* **2019**, *7*, 13650.

[9] K. J. Harry, K. Higa, V. Srinivasan, N. P. Balsara, *J. Electrochem. Soc.* **2016**, *163*, A2216.

[10] S. Yu, D. J. Siegel, *ACS Appl. Mater. Interfaces* **2018**, *10*, 38151.

[11] R. Raj, J. Wolfenstine, *J. Power Sources* **2017**, *343*, 119.

[12] S. S. Shishvan, N. A. Fleck, R. M. McMeeking, V. S. Deshpande, *J. Power Sources* **2020**, *456*, 227989.

[13] Q. Lu, Y. B. He, Q. Yu, B. Li, Y. V. Kaneti, Y. Yao, F. Kang, Q. H. Yang, *Adv. Mater.* **2017**, *29*, 1604460.

[14] H. Duan, Y. X. Yin, Y. Shi, P. F. Wang, X. D. Zhang, C. P. Yang, J. L. Shi, R. Wen, Y. G. Guo, L. J. Wan, *J. Am. Chem. Soc.* **2018**, *140*, 82.

[15] D. Li, L. Chen, T. Wang, L. Z. Fan, *ACS Appl. Mater. Interfaces* **2018**, *10*, 7069.

[16] W. Manalastas, J. Rikarte, R. J. Chater, R. Brugge, A. Aguadero, L. Buannic, A. Llordés, F. Aguesse, J. Kilner, *J. Power Sources* **2019**, *412*, 287.

[17] L. Porz, T. Swamy, B. W. Sheldon, D. Rettenwander, T. Frömling, H. L. Thaman, S. Berendts, R. Uecker, W. C. Carter, Y.-M. Chiang, *Adv. Energy Mater.* **2017**, *7*, 1701003.

[18] E. Kazyak, R. Garcia-Mendez, W. S. LePage, A. Sharafi, A. L. Davis, A. J. Sanchez, K.-H. Chen, C. Haslam, J. Sakamoto, N. P. Dasgupta, *Matter* **2020**, *2*, 1025.

[19] M. Golozar, P. Hovington, A. Paolella, S. Bessette, M. Lagace, P. Bouchard, H. Demers, R. Gauvin, K. Zaghib, *Nano Lett.* **2018**, *18*, 7583

[20] Y. Ren, Y. Shen, Y. Lin, C.-W. Nan, *Electrochem. Commun.* **2015**, *57*, 27.

[21] Federico M. Pesci, R. H. Brugge, A. K. O. Hekselman, A. Cavallaro, R. J. Chater, A. Aguadero, *J. Mater. Chem. A* **2018**, *6*, 19817.

[22] F. Aguesse, W. Manalastas, L. Buannic, J. M. Lopez Del Amo, G. Singh, A. Llordes, J. Kilner, *ACS Appl. Mater. Interfaces* **2017**, *9*, 3808.

[23] L. E. Marbella, S. Zekoll, J. Kasemchainan, S. P. Emge, P. G. Bruce, C. P. Grey, *Chem. Mater.* **2019**, *31*, 2762.

[24] F. Han, A. S. Westover, J. Yue, X. Fan, F. Wang, M. Chi, D. N. Leonard, N. J. Dudney, H. Wang, C. Wang, *Nat. Energy* **2019**, *4*, 187-196.

[25] Q. Li, T. Yi, X. Wang, H. Pan, B. Quan, T. Liang, X. Guo, X. Yu, H. Wang, X. Huang, L. Chen, H. Li, *Nano Energy* **2019**, *63*, 103895.

[26] F. Shen, M. B. Dixit, X. Xiao, K. B. Hatzell, *ACS Energy Lett.* **2018**, *3*, 1056.

[27] N. Seitzman, H. Guthrey, D. B. Sulas, H. A. S. Platt, M. Al-Jassim, S. Pylypenko, *J. Electrochem. Soc.* **2018**, *165*, A3732.

[28] D. S. Eastwood, P. M. Bayley, H. J. Chang, O. O. Taiwo, J. Vila-Comamala, D. J. Brett, C. Rau, P. J. Withers, P. R. Shearing, C. P. Grey, P. D. Lee, *Chem. Commun. (Cambridge, U. K.)* **2015**, *51*, 266.

[29] K. J. Harry, D. T. Hallinan, D. Y. Parkinson, A. A. MacDowell, N. P. Balsara, *Nat. Mater.* **2014**, *13*, 69.

[30] A. Sharafi, H. M. Meyer, J. Nanda, J. Wolfenstine, J. Sakamoto, *J. Power Sources* **2016**, *302*, 135.

[31] E. J. Cheng, A. Sharafi, J. Sakamoto, *Electrochi. Acta* **2017**, 223, 85.

[32] Y. Kim, A. Yoo, R. Schmidt, A. Sharafi, H. Lee, J. Wolfenstine, J. Sakamoto, *Frontiers in Energy Research* **2016**, *4*, 20.

[33] S. Yu, R. D. Schmidt, R. Garcia-Mendez, E. Herbert, N. J. Dudney, J. B. Wolfenstine, J. Sakamoto, D. J. Siegel, *Chem. Mater.* **2015**, *28*, 197.

[34] P. Barai, K. Higa, A. T. Ngo, L. A. Curtiss, V. Srinivasan, *J. Electrochem. Soc.* **2019**, *166*, A1752.

[35] H. Yamada, T. Ito, R. Hongahally Basappa, *Electrochi. Acta* **2016**, *222*, 648.

[36] J. Wolfenstine, H. Jo, Y.-H. Cho, I. N. David, P. Askeland, E. D. Case, H. Kim, H. Choe, J. Sakamoto, *Mater. Lett.* **2013**, *96*, 117.

[37] H.-K. Tian, B. Xu, Y. Qi, *J. Power Sources* **2018**, *392*, 79.

[38] J. J. Bailey, T. M. M. Heenan, D. P. Finegan, X. Lu, S. R. Daemi, F. Iacoviello, N. R. Backeberg, O. O. Taiwo, D. J. L. Brett, A. Atkinson, P. R. Shearing, *J. Microsc.* **2017**, *267*, 384.

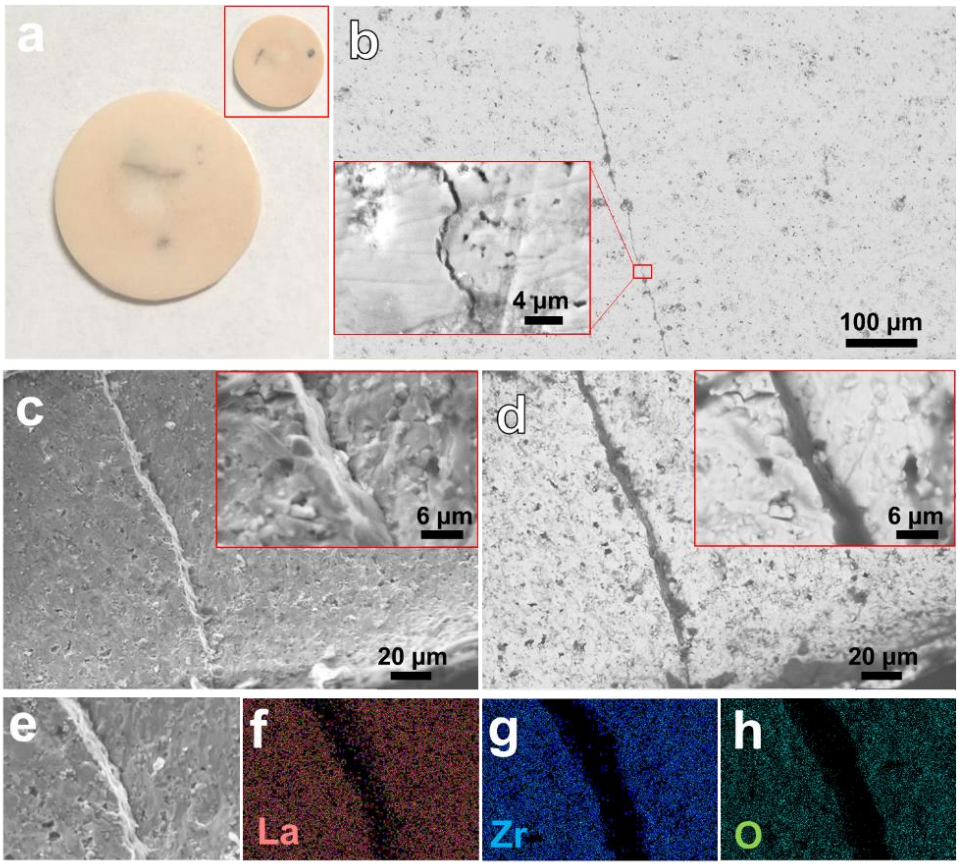

Figure 1. Optical photos (a) and SEM images (b-d) of the short-circuited LLZTO pellet showing a long black line: (a and its inset) optical images of the two sides of the pellet; (b) SEM images of the top surface of the pellet in BSE mode (inset: at higher magnification); SEM images of the cross section of the pellet in SE (c) and BSE (d) modes (insets: at higher magnification). (e-h) SEM-EDS elemental mappings of La, Zr and O in the cross section.

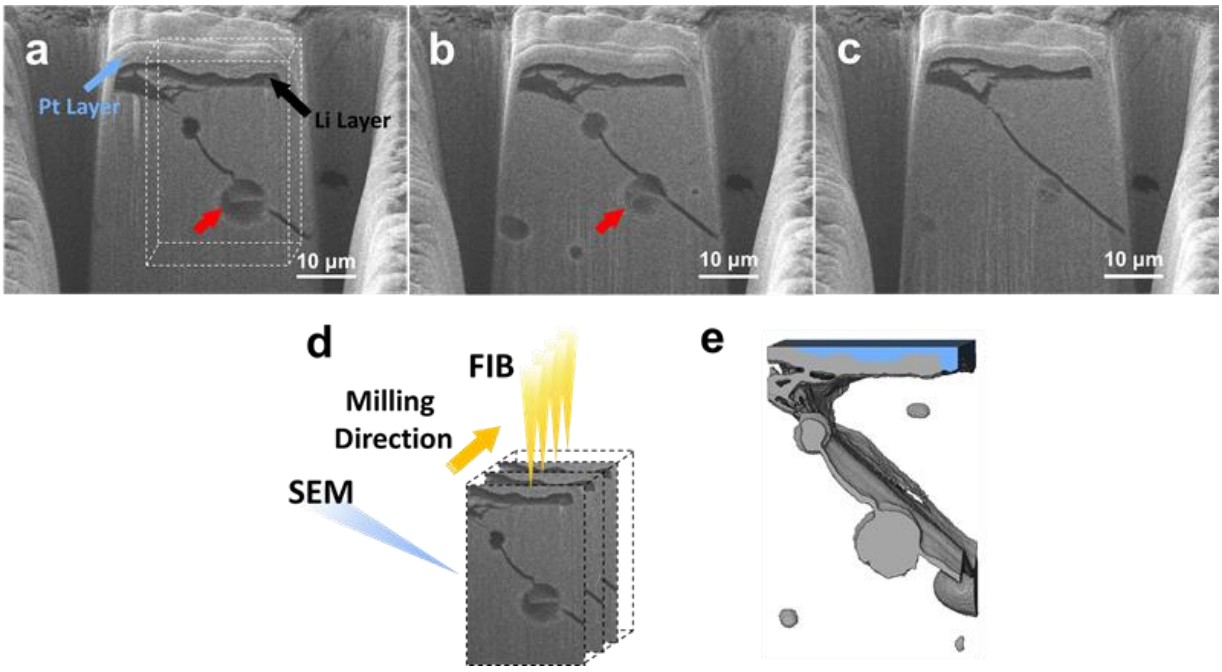

Figure 2. (a-c) Serial SEM images of cross sections of the short-circuited LLZTO pellet after cutting by gallium ion beam for different times: (a) 0 times, (b) 11 times and (c) 16 times; d) schematic image of the process of FIB-SEM "slice-and-view"; e) volume rendering of cracks and pores containing lithium protrusions after segmenting the stacked FIB-SEM slices (cracks and pores are in grey; Pt layer is in blue).

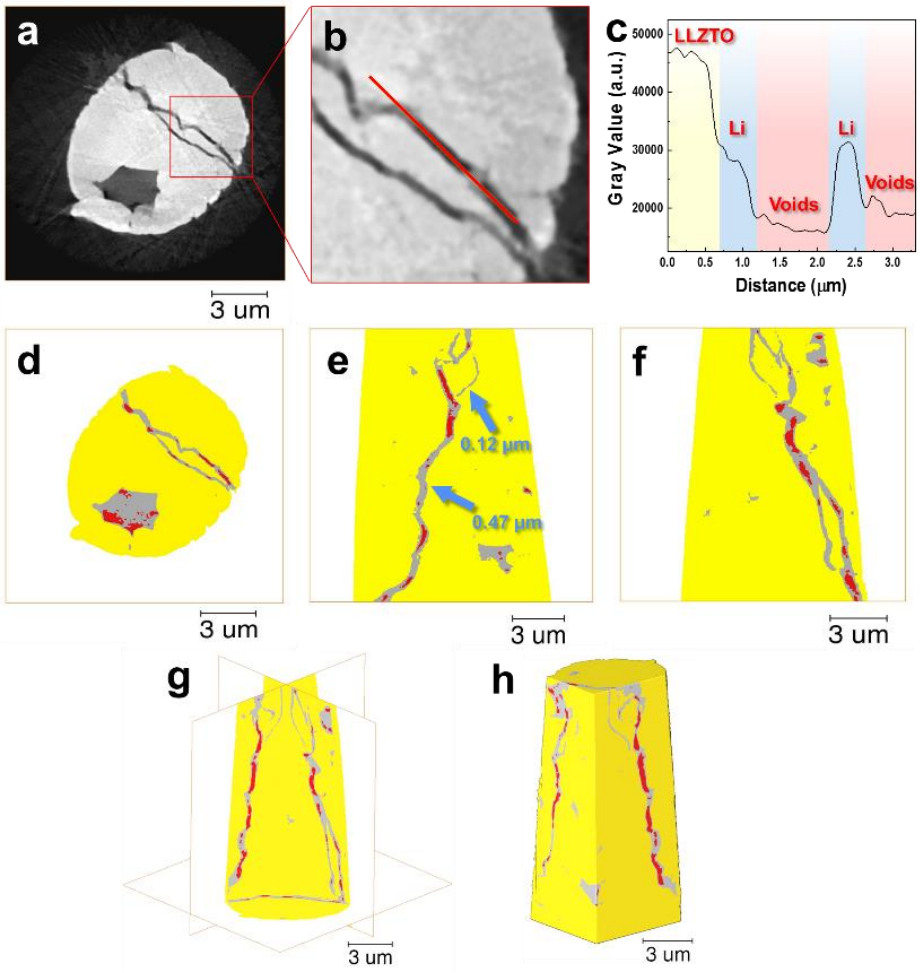

Figure 3. Reconstructed X-ray nano-CT data: a) grayscale slice extracted from a plane perpendicular to the axis of the pillar; b) partial enlargement of (a); c) line profile of the grayscale corresponding to the red line in (b); d) three-phase segmentation of the slice in (a), with the LLZTO in yellow, lithium protrusions in grey and voids in red; cross-sectional slices (e, f) and orthogonal slices (g) after segmentation; h) volume rendering of the pillar with two chopped slices.

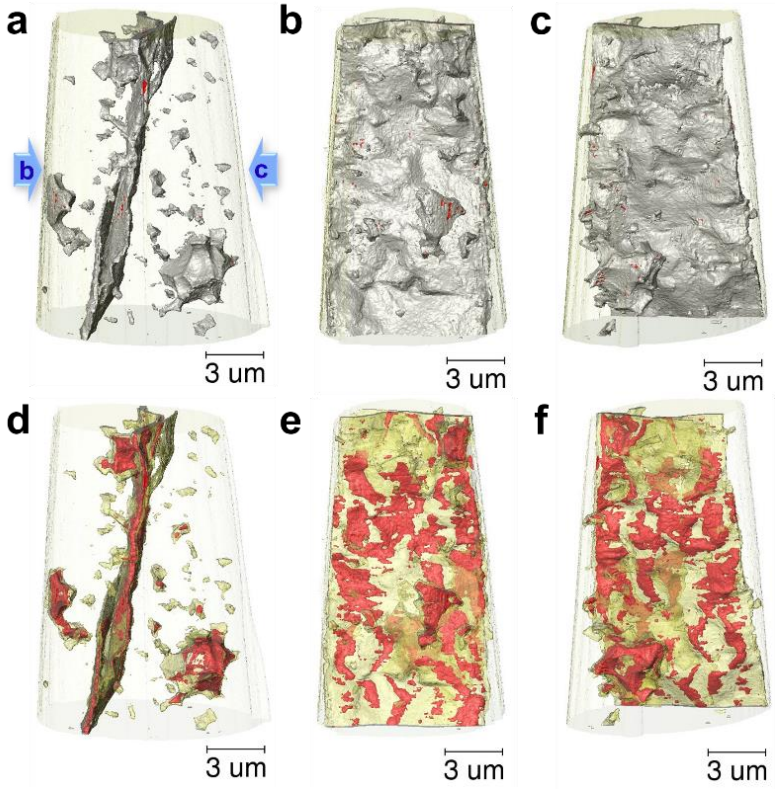

Figure 4. The 3D rendering of the pillar with internal lithium protrusions and voids viewed from three different directions (Fig (a) and (d) are in the same direction; Fig (b) and (e) are in the same direction; Fig (c) and (f) are in the same direction. The viewing directions in Fig (b) and (c) are indicated by the blue arrows in Fig (a).): (a-c) the LLZTO in transparent light yellow, lithium protrusions in opaque grey and voids inside cracks in opaque red; (d-f) the LLZTO in transparent light yellow, lithium protrusion in transparent yellow and voids inside cracks in opaque red.

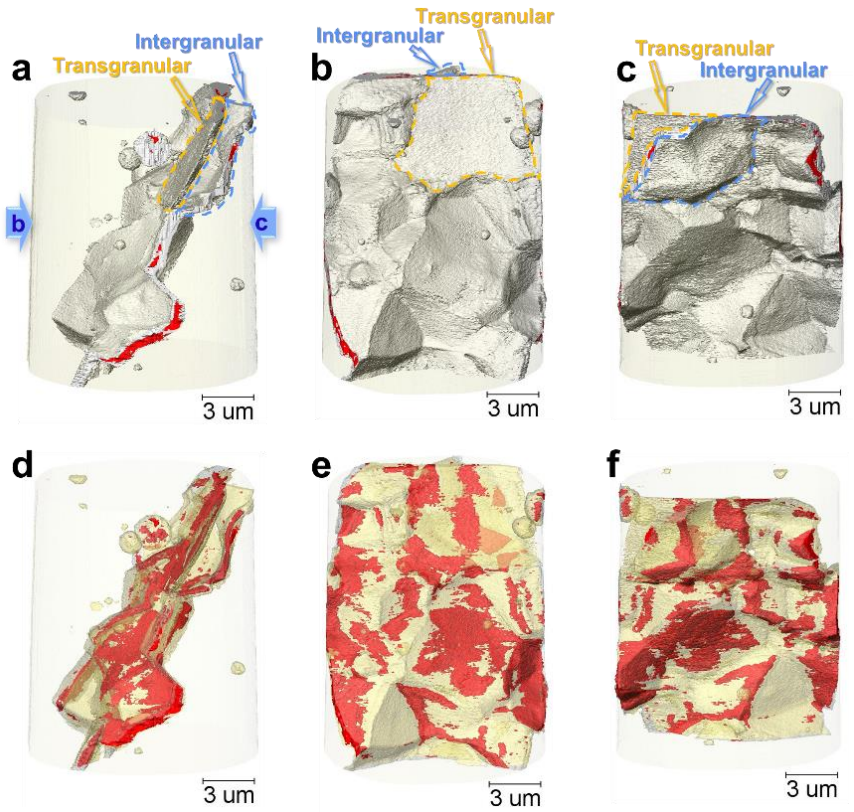

Figure 5. 3D rendering of the lithium protrusions in LLZTO sintered by Field Assisted Sintering, viewed from different directions (Fig (a) and (d) are in the same direction; Fig (b) and (e) are in the same direction; Fig (c) and (f) are in the same direction. The viewing directions in Fig (b) and (c) is indicated by the blue arrows in Fig (a).): (a-c) the LLZTO in transparent light yellow, lithium protrusions in opaque grey and voids inside cracks in opaque red; (d-f) the LLZTO in transparent light yellow, lithium protrusions in transparent yellow and voids inside cracks in opaque red.

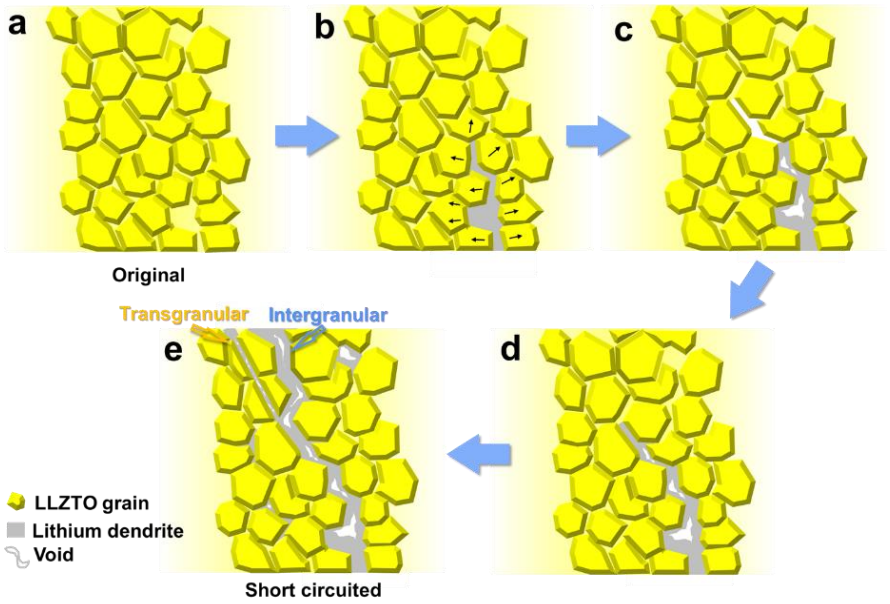

Figure 6. Schematic illustration of the lithium protrusion part-filling in a crack inside LLZTO solid electrolyte: a) original state; b) lithium filling into the grain boundaries or pores; c) cracks widening and propagating under the internal stress; d) lithium filling in the newly-formed crack and e) short-circuited state.

3D Imaging of Lithium Protrusions in Solid-State Lithium Batteries using X-ray Computed Tomography

Shuai Hao, Josh J. Bailey, Francesco Iacoviello, Junfu Bu, Patrick S. Grant, Dan J. L. Brett and Paul R. Shearing*

Table of Contents Figure

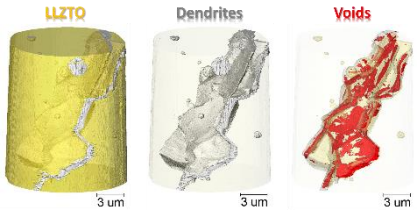

By utilizing high-resolution X-ray nano-CT, the morphology of lithium protrusions in short-circuited garnet-based solid electrolytes is successfully distinguished in three dimensions. The lithium protrusions partially fill cracks, leaving voids preferentially in regions of larger curvature. They together form a waved plane in a geometry largely templated to the grain boundaries, which primarily propagate intergranularly through the solid electrolyte, meanwhile occasionally form flat branches in a transgranular mode.